Large Inverse Spin Hall Effect in Co-Pt Spin-Valve Heterostructures

X. L. Zheng,[1,2] L. K. Zou,[1] Y. Zhang,[1] and J. W. Cai[1,2,*]

[1]*Beijing National Laboratory for Condensed Matter Physics, Institute of Physics, Chinese Academy of Sciences, Beijing 100190, People's Republic of China*

[2]*School of Physical Sciences, University of Chinese Academy of Sciences, Beijing 100049, People's Republic of China*

(Received 10 October 2016; revised manuscript received 16 January 2017; published 6 April 2017)

By using the $Y_3Fe_5O_{12}$ (YIG)/Cu/$Co_{0.65}Pt_{0.35}$ pseudo-spin-valve (SV) heterostructure, we identify the large inverse spin Hall effect (ISHE) from Co-Pt together with the conventional anomalous Nernst effect and anomalous Righi-Leduc effect. When thin ferromagnetic (FM) Co-Pt layers are exchanged coupled by an additional antiferromagnetic (AFM) Ir-Mn layer, the well-separated ISHE signal generated in the Co-Pt layer is significantly enhanced because the spin current coming from the YIG and produced by the Co-Pt itself is mostly reflected at the Co-Pt surface for the pseudo-SV heterostructure but absorbed by the AFM Ir-Mn layer in the exchange-bias SV samples. The SV heterostructure with a soft Co layer also gives a distinguishable ISHE signal but with much smaller magnitude. The present results show that the metallic FM-AFM structure is an efficient spin-current detector. In addition, FM metals alloyed with heavy elements like Pt are beneficial to spin-orbit coupling-correlated phenomena, including ISHE and the anomalous Hall effect.

DOI: 10.1103/PhysRevApplied.7.044003

I. INTRODUCTION

In recent years, the generation, manipulation, and detection of pure spin currents have attracted a great deal of attention in spintronics [1–6]. Heat currents also interact with spin currents; this has spawned the field of spin caloritronics, where one explores the interplay of spin, charge, and heat and further exploits potential applications [7]. The spin Seebeck effect (SSE) within the framework of spin caloritronics refers to the spin current generated from a ferromagnetic (FM) metal, semiconductor, or insulator by a temperature gradient [8–10], which is originally detected in the Pt strip patterned onto these different FM materials through the Pt inverse spin Hall effect (ISHE). It is known that there are two ways to observe the SSE using either the transverse or the longitudinal SSE configuration with a temperature gradient applied in the sample plane or out of plane, respectively. However, the mechanisms responsible for the observed magnetothermoelectric signal in the heterostructures are found to be rather complicated and controversial. In addition to the SSE, the anomalous and planar Nernst effects (ANE and PNE) [11–14] as well as the anomalous and planar Righi-Leduc effects (ARLE and PRLE) [15,16] also present for the transverse SSE configuration. In the longitudinal SSE (LSSE) using Pt on a FM insulator, the ANE due to the magnetic proximity effect in Pt is entangled with the SSE [17,18]. Fortunately, the heterostructure containing a nonmagnetic (NM) heavy metal and a FM insulator that is free from the magnetic proximity effect unequivocally ascertains the intrinsic LSSE [19–21], which offers a simple methodology to investigate spin-current phenomena.

A variety of NM heavy metals possessing large spin Hall angles are adopted to detect the thermally excited spin current in LSSE [22]. Under the perpendicular temperature gradient, ferromagnetic films of permalloy (Py) have also been identified to generate appreciable ISHE signals by comparing the thermal voltages in the insulating $Y_3Fe_5O_{12}$(YIG)/Py samples with and without a spin-current blocking layer [23]. This pioneering work opens another avenue to exploit spin-current phenomena. It should be pointed out that FM conductors have the thermoelectric transport properties of the ANE and PNE, which correspond to the transverse thermal voltage developed in response to a heat current for perpendicular and in-plane magnetization, respectively. Meanwhile, FM metals also show thermomagnetic properties of the ARLE and PRLE, referring to the transverse temperature gradient developed in response to a heat current with perpendicular and in-plane magnetization, respectively [15,16]. Therefore, for a heterostructure containing a FM insulator and a FM metal with the LSSE configuration, the perpendicular temperature gradient ∇T_z will generate not only the ISHE voltage but also the ANE and ARLE signals with

$$V_{\mathrm{ISHE}} \propto \theta_{\mathrm{SH}} \vec{J}_S \times \vec{\sigma}, \tag{1}$$

$$V_{\mathrm{ANE}} \propto \vec{M} \times \nabla T_z, \tag{2}$$

*Corresponding author.
jwcai@aphy.iphy.ac.cn

$$\nabla T_x \propto \vec{M} \times \vec{J}_Q, \tag{3}$$

where θ_{SH} is the spin Hall angle of the FM metal, $\vec{\sigma}$ is the polarization direction of the perpendicularly injected spin current $\vec{J}_S$, which depends on the magnetization orientation of the FM insulator (e.g., YIG), whereas $\vec{M}$ is the magnetization vector of the FM metal, $\vec{J}_Q$ is the heat current in the FM metal by ∇T_z, and ∇T_x is the transverse temperature gradient generated by $\vec{J}_Q$ due to the ARLE, leading to a voltage signal (V_{ARLE}) proportional to ∇T_x because of the thermocouple effect [16]. Experimentally, it is difficult to discriminate between the ANE and ARLE (and between the PNE and PRLE). One can take them as a whole when dealing with the thermally excited spin current and the corresponding ISHE, and from Eqs. (1)–(3), the ISHE voltage can be directly separated from the ANE and ARLE signals if the FM insulator and the FM metal in the heterostructure switch their magnetizations at distinctly different fields. Wu *et al.* [24] developed a magnetically decoupled $Fe_3O_4/Ti/Co_{0.2}Fe_{0.6}B_{0.2}$ trilayer structure to study the ISHE of the soft (Co,Fe)B films by taking advantage of the relatively large coercivity of the Fe_3O_4 film. The drawback of this structure is that the required insulating property with a negligible ANE for the Fe_3O_4 film is achieved only at very low temperature. As an excellent pure spin-current source and ideal spin-transport carrier with extremely low magnetic damping [25,26], the electrically insulating YIG film is magnetically soft. Tian *et al.* [27] utilized the relatively large coercivity of the very thin Co layers to isolate its ISHE in the YIG/Cu/Co structure. However, this structure is no more valid once the Co-layer thickness exceeds 5 nm because of its insufficient coercivity.

As is known, when Co is alloyed with Pt, its magnetocrystalline anisotropy and coercivity increase considerably with maximum values appearing in Co-Pt films at around 20-at. % Pt without considering the $L1_0$-ordered equiatomic Co-Pt that requires high-temperature annealing [28,29]. On the other hand, exchange coupling between FM and antiferromagnetic (AFM) layers can shift hysteresis loops significantly [30,31]. This exchange-bias phenomenon is widely adopted to engineer magnetics in the conventional spintronic devices of spin valves (SVs) and magnetic tunnel junctions (MTJs) [32,33]. In addition, most AFM materials are found to possess appreciable SHE with very short spin-diffusion length [34–37]. In this article, we report on the LSSE in the YIG/Cu/Co-Pt and YIG/Cu/Co-Pt/Ir-Mn heterostructures. Large ISHE voltage is unambiguously separated from the conventional ANE and/or ARLE signals in the pseudo-SV heterostructure. Most remarkably, the appreciable ISHE signal generated in the thin Co-Pt layers is further greatly enhanced in the exchange-biased SV heterostructure because the spin current coming from the YIG and produced by the Co-Pt itself is mostly reflected at the Co-Pt surface in the pseudo-SV heterostructure but absorbed by the AFM Ir-Mn layer in the SV samples. We also extend the exchange-biased SV heterostructure to the case of Co with small coercivity, which gives a much smaller but still rather distinguishable ISHE. Our results show that the exchange-biased FM metal films can be an effective and reliable structure to detect spin current. In addition, FM metals alloyed with a heavy element like Pt are beneficial to spin-orbit coupling-correlated phenomena, including ISHE and anomalous Hall effect (AHE).

II. EXPERIMENT

The single-crystal ferrimagnetic (111) YIG films with thickness of 13 μm are grown by liquid-phase epitaxy onto a (111) $Gd_3Ga_5O_{12}$ (GGG) substrate. Using dc magnetron sputtering, and metallic multilayers are deposited at ambient temperature on the YIG films ($5 \times 3 \times 0.5$ mm^3) cut from the same YIG specimen. The samples include (1) YIG/Cu(0.8–5 nm)/Co-Pt(3–15 nm), (2) YIG/Cu(0.8–5 nm)/Co-Pt(3–10 nm)/Ir-Mn(8 nm), and (3) YIG/Cu(3.5 nm)/Co(5 nm)/Ir-Mn(8 nm).

For comparison, the metallic multilayer films and the Co-Pt(5 nm) and Co(5 nm) single-layer films are also deposited on the GGG substrates ($5 \times 3 \times 0.5$ mm^3). In order to protect the metallic layers from oxidation, all samples are finally covered with a 5-nm SiO_2 layer *in situ* by rf sputtering. The respective compositions of Co-Pt and Ir-Mn films determined by inductively coupled plasma (ICP)–atomic emission spectroscopy (AES) are $Co_{0.65}Pt_{0.35}$ and $Ir_{0.22}Mn_{0.78}$ in atomic percent. The base pressure of the sputtering system is better than 4.0×10^{-5} Pa, and the working argon pressure is 0.5 Pa. A shadow mask is used to pattern the sputtering-deposited layers into the Hall-bar shape for transport measurements. Each Hall bar includes a 4.8×0.5 mm^2 channel with three perpendicularly placed 1.5×0.3 mm^2 side bars 1.7 mm apart. In order to induce an easy magnetization axis and exchange bias in the Co-Pt layers, a static field of about 300 Oe is applied parallel to the side bars during sputtering.

The magnetic properties of the YIG and metallic films at room temperature are characterized using a vibrating sample magnetometer (VSM). For the LSSE measurements shown in Fig. 1(a), the temperature gradient ∇T_z is on the z axis normal to the film plane with a temperature difference of about 13 K between the sample surface and bottom. The film surface in thermal contact with the heat sink is maintained at a constant temperature of about 300 K. The external field H is applied on the y axis (parallel to the magnetic easy axis and exchange-bias direction). The thermal voltage through the Hall-bar channel on the x axis is measured by the two end electrodes. Ultrasonic wire bonding (20 μm in diameter) is used for electrode connection. It should be pointed out that the perpendicular temperature gradient is accomplished by placing the samples ($5 \times 3 \times 0.5$ mm^3) between, and in thermal

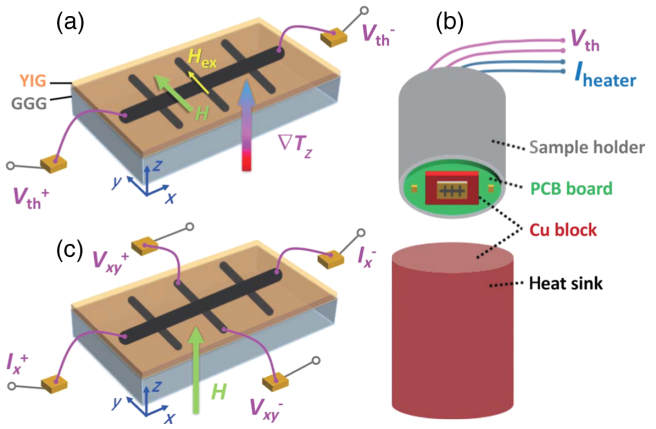

FIG. 1. (a) Schematic diagram of the Hall-bar sample used for the longitudinal spin Seebeck effect measurement, with the temperature gradient (on the z axis) applied perpendicularly to the film plane (on the x-y plane), the external field H applied on the y axis, which is also parallel to the magnetic easy axis and exchange-bias direction (H_{ex}), and the thermal voltage measured through the Hall-bar channel (on the x axis) by the two end electrodes. (b) Schematic diagram of the vertical temperature gradient generating system assembly for the longitudinal spin Seebeck effect measurement. (c) Anomalous Hall effect measurement with the electric current flowing along the Hall-bar channel (on the x axis), the external field H applied on the z axis, and the anomalous Hall voltage measured by the two side electrodes (on the y axis).

contact with, two Cu blocks at two different temperatures, as we describe in Fig. 1(b). One Cu block is cylinder shaped with a diameter of 30 mm and height of 125 mm, and it acts as the heat-sinking end. The other Cu block is rectangular in shape with dimensions $13 \times 9 \times 1.5$ mm^3. A Pt 100-Ω heater ($5 \times 2 \times 1$ mm^3) is symmetrically fixed at the center of the Cu block back using silver paint. This Cu block is symmetrically fixed on a circular printed circuit board (PCB) (26 mm in diameter) with a rectangular hole (9×4 mm^2) in the center. The PCB itself is fixed to the sample holder through four ceramic rods (4 mm in diameter, 6 mm in height). The sample and the two Cu blocks are symmetrically stacked along the vertical central axis to eliminate any in-plane heat current in the sample. The whole thermal assembly is finally placed on a horizontally rotatable stage. The experimental configuration for the AHE measurement is described in Fig. 1(c). The electric current flows along the Hall-bar channel on the x axis, the external field H is applied on the z axis perpendicular to the film plane, and the Hall voltage is measured by the two side electrodes along the y axis.

III. RESULTS AND DISCUSSION

The results of the YIG/Cu/Co-Pt samples are presented first. Since the nanometer-thick Co-Pt layer is 3 orders thinner than the YIG film in the current YIG/Cu/Co-Pt structure, the magnetic signal from the Co-Pt layer is submerged by the huge YIG signal for the VSM measurement. The magnetic properties of YIG and Co-Pt films are, thus, characterized from the single-layer YIG film and the GGG substrate/Cu/Co-Pt bilayer, respectively. Figures 2(a) and 2(b) display representative M-H loops. The YIG film is magnetically soft and isotropic in the film plane with the saturation field less than 30 Oe. Its perpendicular hysteresis loop dominated by the shape anisotropy is saturated around 1.75 kOe, close to the YIG saturation magnetization. The perpendicular remanent magnetization ratio is below 2%, which means that the out-of-plane magnetization of the

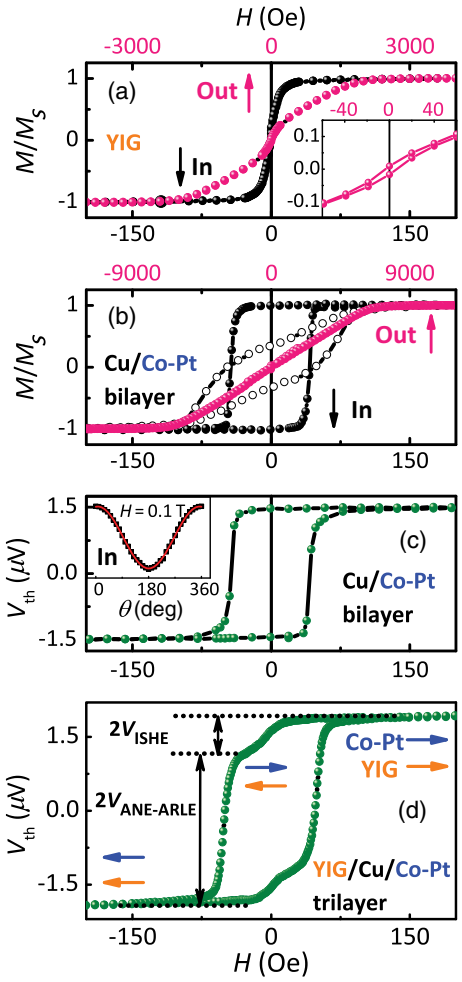

FIG. 2. In-plane and out-of-plane M-H curves of (a) single-layer YIG film, (b) GGG/Cu(3 nm)/Co-Pt(5 nm) film with the in-plane field along the magnetic easy (solid circle) and hard (hollow circle) axes. The in-plane loop is scaled in the number of the bottom x axis, whereas the perpendicular loop is scaled in the number of the top x axis. The inset of (a) is a magnified view of the perpendicular loop in small fields. Field dependence of thermal voltage V_{th} for (c) GGG/Cu(3 nm)/Co-Pt(5 nm) and (d) YIG/Cu(3 nm)/Co-Pt(5 nm). The inset of (c) shows the angular dependence of thermal voltage in a constant in-plane field of 1.0 kOe. The experimental data can be perfectly fitted by a $\cos\theta$ function.

YIG film is negligible near zero field. On the other hand, the 5-nm Co-Pt film is magnetically anisotropic in the film plane. It exhibits a rather square in-plane hysteresis loop with the external field parallel to the growth field direction (magnetic easy axis). The coercivity (H_c) is about 45 Oe. Orthogonal to the easy axis, the in-plane M-H curve at the hard axis is slanted with coercivity of about 45 Oe and saturation field of about 120 Oe. The perpendicular hysteresis loop of the Co-Pt film is saturated at a field as high as 7 kOe with negligible remanence. It should be emphasized that because of the large magnetocrystalline anisotropy, all Co-Pt films with the studied thickness from 3 to 15 nm show similar M-H loops with little change in coercivity at the easy axis. One can expect that magnetically the YIG/Cu/Co-Pt structure will exhibit pseudo-spin-valve-like behavior; i.e., the YIG switches its magnetization at small fields, whereas the Co-Pt magnetization cannot be altered until larger fields when the external field is applied at the magnetic easy axis.

The thermal voltage of the control sample GGG/Cu(3 nm)/Co-Pt(5 nm) is examined using the LSSE setup. The corresponding result is shown in Fig. 2(c). One can note that the square $V_{\rm th}$-H loop resembles the easy-axis magnetic hysteresis loop, where a large sharp change in thermal voltage coincides with the rapid switching of the Co-Pt magnetization at the coercivity. Such a characteristic thermal voltage should originate from the ANE and/or ARLE signals of the Cu/Co-Pt film, $V_{\rm ANE\text{-}ARLE}$. In order to rule out other possible contributions, e.g., PNE and PRLE, etc., the dependence of the thermal voltage as a function of the Co-Pt magnetization direction (θ) is further examined by rotating the whole sample stage in a constant in-plane field of 1.0 kOe. The inset of Fig. 2(c) shows the $V_{\rm th}$-θ curve of the control sample. The experimental data can be perfectly fitted by a $\cos\theta$ function without any component of $\sin\theta\cos\theta$. Since the ANE and/or ARLE signal has a $\cos\theta$ dependence, whereas the PNE and/or PRLE signal shows a $\sin\theta\cos\theta$ dependence [12,16], the angular dependence result suggests that the measured thermal voltage should not contain any contribution from PNE or PRLE, and the in-plane heat current in the sample is indeed negligible for the present setup. As for the thermal measurement results of the YIG/Cu/Co-Pt structure, multiple changes in thermal voltage are found at distinct fields corresponding to YIG and Co-Pt magnetization switching. Figure 2(d) shows the field dependence of thermal voltage $V_{\rm th}$ for YIG/Cu(3 nm)/Co-Pt(5 nm). In addition to the ANE and ARLE signals, the additional thermal voltage change should come from the SSE (or ISHE) because of the spin current from YIG. Before detailing this result, we stress that in the present LSSE setup, there is no in-plane heat current. In addition, both YIG and Co-Pt layers have almost zero perpendicular magnetization near zero field. It is not possible that the ISHE voltage corresponding to the YIG switching will have contribution from the ARLE and/or PRLE of the Cu/Co-Pt layer.

From Fig. 2(d), one notes that at large positive fields, the moments of the YIG and Co-Pt layers are aligned at the same (set as right) direction. The measured thermal voltage $V_{\rm th} = V_{\rm ISHE} + V_{\rm ANE\text{-}ARLE}$ does not present any variation for $H > 30$ Oe. When the external field varies downward from 30 to -30 Oe, the hard Co-Pt moment remains at the right direction, but the YIG moment switches to the left direction. This means the $V_{\rm ANE\text{-}ARLE}$ is unchanged, whereas the $V_{\rm ISHE}$ is reversed; consequently, the measured thermal voltage changes to $V_{\rm th} = -V_{\rm ISHE} + V_{\rm ANE\text{-}ARLE}$. The thermal voltage variation solely caused by the YIG moment switching or the ISHE gives the value of $V_{\rm ISHE} \approx 0.38\ \mu$V. When the external field further decreases from -30 to -100 Oe, the Co-Pt moment also switches to the left direction, whereas the YIG moment remains at the left direction. The measured thermal voltage, thus, becomes $V_{\rm th} = -V_{\rm ISHE} - V_{\rm ANE\text{-}ARLE}$ with the $V_{\rm ANE\text{-}ARLE}$ being reversed. The total voltage variation merely caused by the Co-Pt moment switching or the ANE-ARLE, reflects the value of $V_{\rm ANE\text{-}ARLE} \approx 1.54\ \mu$V. There is no more change for the thermal voltage at larger negative fields, consistent with the aligned YIG and Co-Pt moments at the left direction. As the external field switches back, the thermal voltage presents the other branch of the closed loop, in accordance with the switching back of the Co-Pt and YIG moments in sequence.

Other samples with the YIG/Cu/Co-Pt structure mostly show a similar thermal voltage loop with separated ISHE and ANE and/or ARLE signals, depending on the Cu and Co-Pt thicknesses. We point out that the Cu spacer should be neither too thin nor too thick in order to optimize the ISHE signal. As is known, in magnetic multilayers there exists an interlayer coupling between the magnetic layers, including direct exchange coupling through pin holes, orange peel magnetostatic coupling because of the film roughness, and indirect interlayer exchange coupling due to the quantum-well effect [38]. When the Cu spacer is below 2 nm, the Co-Pt and YIG layers switch their magnetization almost simultaneously because of the increased interlayer coupling, which make the ISHE and ANE and/or ARLE signals indistinguishable. On the other hand, although the spin current can pass through a relatively thick Cu spacer with negligible ISHE voltage in the Cu layer because Cu has a very large spin-diffusion length (on the order of hundreds of nanometers) and very weak spin-orbit coupling, the highly conductive Cu spacer at large thickness greatly diminishes both the ISHE and ANE and/or ARLE voltages, especially the former. When the Cu thickness exceeds 5 nm, it becomes difficult to extract the tiny ISHE signal from the thermal voltage. Therefore, the suitable Cu thickness ranges between 2 and 5 nm for the present experiment. Below, the different YIG/Cu/Co-Pt samples with Cu spacer thickness fixed at 3 nm are detailed.

Earlier, we demonstrate the YIG/Cu(3 nm)/Co-Pt(5 nm) to exhibit large ISHE and ANE and/or ARLE signals with $V_{\mathrm{ISHE}} \approx 0.38\ \mu$V and $V_{\mathrm{ANE\text{-}ARLE}} \approx 1.54\ \mu$V. When the Co-Pt layer increases to 10 nm, the V_{ISHE} decreases to 0.28 μV, but the $V_{\mathrm{ANE\text{-}ARLE}}$ increases to 2.29 μV, and the V_{ISHE} becomes only a tiny fraction of the $V_{\mathrm{ANE\text{-}ARLE}}$. Our results suggest that a relatively thin Co-Pt layer is more suitable for spin-current detection. Figure 3(a) shows the Co-Pt thickness dependences of the ISHE and the ANE and/or ARLE voltages directly determined from the thermal voltage loops. One notes that the V_{ISHE} decreases, whereas the $V_{\mathrm{ANE\text{-}ARLE}}$ increases when the Co-Pt thickness varies from 3 to 15 nm. The Co-Pt spin-diffusion length (λ_{SD}) is about 2.1 nm, which we determine later. Since the thermally injected spin current in FM metals for ISHE voltage generation exponentially decays with the FM metal thickness (t) by $\exp(-t/\lambda_{\mathrm{SD}})$, it is reasonable that the measured V_{ISHE} monotonically decreases with the Co-Pt thickness. As for the ANE or ARLE voltage, it takes place in the whole FM metal layer regardless of its dimension, which means that the *primary* ANE and/or ARLE voltage induced in the Co-Pt layer should change little for the relatively thick Co-Pt layer with a negligible surface-interface effect. Using an equivalent parallel circuit with the Cu shunting taken into account [27], we estimate the ANE and/or ARLE voltage primarily generated in the Co-Pt layer based on the directly measured $V_{\mathrm{ANE\text{-}ARLE}}$, the heterostructure resistance, and the Cu spacer resistance obtained in a 3-nm Cu single-layer sample. Indeed, the calculated *primary* ANE-ARLE voltage is almost independent of the Co-Pt thickness when exceeding 5 nm. Therefore, the increase of the measured $V_{\mathrm{ANE\text{-}ARLE}}$ in Fig. 3(a) is due to the relatively less Cu shunting for thicker Co-Pt layers.

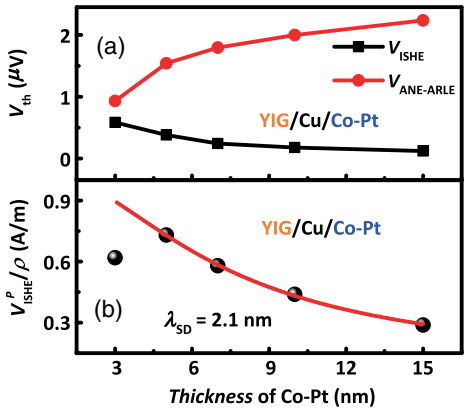

FIG. 3. (a) Co-Pt thickness dependences of the ISHE and the ANE or ARLE voltages directly determined from the thermal voltage loops for the series samples. (b) The *primary* ISHE voltage (V^{p}_{ISHE}) generated in the Co-Pt layer divided by its resistivity (ρ) as a function of the Co-Pt thickness. Black circle corresponds to experimental data and red line denotes the fitting result with Eq. (4).

The *primary* ISHE voltage (V^{p}_{ISHE}) generated in Co-Pt and the corresponding Co-Pt layer resistivity (ρ) are also estimated through the simple parallel circuit. Figure 3(b) plots the Co-Pt thickness (t) dependence of $V^{p}_{\mathrm{ISHE}}/\rho$ for the YIG/Cu(3 nm)/Co-Pt series samples. According to the thermally induced spin-current injection model [39], the V^{p}_{ISHE} should obey the equation

$$V^{p}_{\mathrm{ISHE}} = 2(CL\nabla T)(\rho\theta_{\mathrm{SH}})[(\lambda_{\mathrm{SD}}/t)\tanh(t/2\lambda_{\mathrm{SD}})], \quad (4)$$

where C is the spin-current injection coefficient, L is the length of the Hall bar, ∇T is the temperature gradient, and θ_{SH} and λ_{SD} are the respective spin Hall angle and spin-diffusion length of the Co-Pt alloy. Note that the experimental data can be well described by Eq. (4) except for the thinnest Co-Pt sample. From the data fitting, λ_{SD} is determined to be about 2.1 nm. By assuming the same C for similar hybrid structures, the thermal spin-current injection model yields reasonable relative values of the spin Hall angle for transition metals [39]. In order to obtain the spin Hall angle of the Co-Pt alloy, we prepare a control sample of YIG/Cu(3 nm)/Pt(5 nm). The thermal measurement gives $V_{\mathrm{ISHE(Pt)}} \approx 1.64\ \mu$V, appreciably larger than $V_{\mathrm{ISHE(Co\text{-}Pt)}} \approx 0.38\ \mu$V for the YIG/Cu(3 nm)/Co-Pt(5 nm). Taking into account the Cu shunting, the *primary* ISHE voltage and resistivity are estimated as $V^{p}_{\mathrm{ISHE(Co\text{-}Pt)}} \approx 0.46\ \mu$V, $V^{p}_{\mathrm{ISHE(Pt)}} \approx 1.97\ \mu$V, and $\rho_{\mathrm{(Co\text{-}Pt)}} \approx 52.0\ \mu\Omega\,$cm, $\rho_{\mathrm{(Pt)}} \approx 40.3\ \mu\Omega\,$cm for the corresponding samples. With $\lambda_{\mathrm{SD(Co\text{-}Pt)}} \approx 2.1$ nm, and $\lambda_{\mathrm{SD(Pt)}} \approx 2.5$ nm [39]. We obtain $\theta_{\mathrm{SH(Co\text{-}Pt)}} \approx 0.2\theta_{\mathrm{SH}(Pt)}$. This value is smaller than those of Pt, Ta, and W [40].

Considering the key role of AFM-FM exchange bias in conventional SVs and MTJs and the fact that AFM thin films possess appreciable SHE [34–37], an AFM Ir-Mn layer is further adopted to magnetically pin the Co-Pt layer of the heterostructure. Magnetic measurement of the GGG/Cu(3 nm)/Co-Pt(5 nm)/Ir-Mn(8 nm) sample gives a square M-H loop ($H_c = 47$ Oe) offset at -175 Oe, and this exchange-bias field inversely varies with the Co-Pt thickness. The out-of-plane hysteresis loops change very little compared with those without the AFM Ir-Mn layer; namely, the exchange-biased Co-Pt layers still have negligible out-of-plane magnetization near zero field. Taking into account the magnetic measurement results together with the negligible in-plane heat current in the thermal measurement setup, neither PNE nor PRLE will present in the heterostructure with the additional AFM Ir-Mn layer. Figures 4(a) and 4(b) show the field dependence of thermal voltage for representative samples of YIG/Cu(3 nm)/Co-Pt/Ir-Mn(8 nm) with Co-Pt thickness at 5 and 10 nm. For comparison, the field dependence of the thermal voltage of GGG/Cu(3 nm)/Co-Pt/Ir-Mn(8 nm) with the same Co-Pt thicknesses is displayed in Figs. 4(c) and 4(d). One can clearly observe two very large voltage signals in

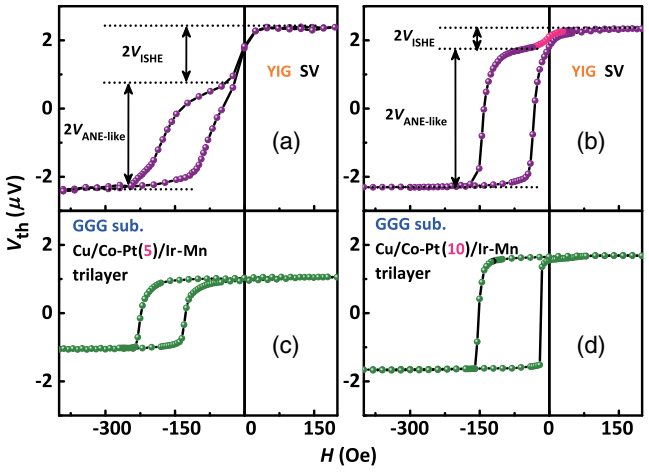

FIG. 4. Field dependence of thermal voltage V_{th} for (a) YIG/Cu(3 nm)/Co-Pt(5 nm)/Ir-Mn(8 nm), (b) YIG/Cu(3 nm)/Co-Pt(10 nm)/Ir-Mn(8 nm), (c) GGG/Cu(3 nm)/Co-Pt × (5 nm)/Ir-Mn(8 nm), and (d) GGG/Cu(3 nm)/Co-Pt(10 nm)/Ir-Mn(8 nm).

the SV samples corresponding to the YIG and Co-Pt magnetization switching around zero field and at large negative field, respectively. As is known, the internal spins of the AFM layer do not respond with the applied field due the lack of the net moment. This part will not generate any ANE or ARLE voltage under the perpendicular temperature gradient. The interfacial AFM moment might be changed by the external field in accordance with the Co-Pt magnetization due to the exchange-spring effect [41]; therefore, the tiny ANE-ARLE of the AFM layer ($V^{\text{Ir-Mn}}_{\text{ANE-ARLE}}$, if any) should coincide with the ANE-ARLE in the Co-Pt layer. Since the ARLE voltage strongly depends on the electrode materials [16], the ARLE signal in the YIG/Cu/Co-Pt/Ir-Mn and GGG/Cu/Co-Pt/Ir-Mn samples can be modified compared with the samples without the Ir-Mn layer, but it should be stressed that the ARLE signal will always follow the Co-Pt magnetization switching as the ANE does. We point out that different from the case of the pseudo-SV samples, each thermal voltage signal for the SV structure has more contributions. Comprehensively considering all magnothermoelectric voltages generated in the SV sample, the signal around zero field should be contributed by $V^{\text{YIG/Co-Pt}}_{\text{ISHE}}$ and $V^{\text{YIG/Ir-Mn}}_{\text{ISHE}}$, i.e., the ISHE voltages in the Co-Pt and Ir-Mn layers generated by the spin current from the YIG, which is the central issue of the present paper. The other signal at negative field should be contributed by $V^{\text{Co-Pt/Ir-Mn}}_{\text{ISHE}}$, $V^{\text{Co-Pt}}_{\text{ANE-ARLE}}$, and $V^{\text{Ir-Mn}}_{\text{ANE-ARLE}}$. That is, the ISHE voltage in the Ir-Mn layer due to the spin current produced by the Co-Pt, the ANE-ARLE voltage inherent to the Co-Pt, and the ANE-ARLE voltage due to the AFM exchange spring. Since $V^{\text{Co-Pt/Ir-Mn}}_{\text{ISHE}}$, $V^{\text{Co-Pt}}_{\text{ANE-ARLE}}$, and $V^{\text{Ir-Mn}}_{\text{ANE-ARLE}}$ are proportional to the Co-Pt magnetization, it is impossible to directly separate them in the SV structure. Hereafter, in the description of the thermal voltage of the SV heterostructure, the phrase "ANE-like voltage" ($V_{\text{ANE-like}}$) is used to represent them, whereas the ISHE voltage (V_{ISHE}) refers only to $V^{\text{YIG/Co-Pt}}_{\text{ISHE}}$ and $V^{\text{YIG/Ir-Mn}}_{\text{ISHE}}$ that are caused by the YIG spin current without any artifact. Parenthetically, we fabricate two additional samples on Si substrates and measure their thermal voltage (V_{th}) and resistance (R) as (1) Si/Cu(3 nm)/Co-Pt(5 nm)/SiO_2(5 nm) with $R \approx 572\,\Omega$, and $V_{\text{th}} = V^{\text{Co-Pt}}_{\text{ANE-ARLE}} \approx 1.09\ \mu\text{V}$ and (2) Si/Cu(3 nm)/Co-Pt(5 nm)/Ir-Mn(8 nm)/SiO_2(5 nm) with $R \approx 346\,\Omega$ and $V_{\text{th}} \approx 0.83\ \mu\text{V}$.

Assuming that $V^{\text{Co-Pt}}_{\text{ANE-ARLE}}$ and the resistance of the individual layers are unvaried in the metallic bilayer and trilayer and $V^{\text{Ir-Mn}}_{\text{ANE-ARLE}}$ is negligible, we obtain $V^{\text{Co-Pt/Ir-Mn}}_{\text{ISHE}} \approx 0.65\ \mu\text{V}$ for the Si/Cu/Co-Pt/Ir-Mn sample through the parallel circuit. This roughly estimated result reflects the significant ISHE voltage in the Ir-Mn layer due to the spin current produced by the Co-Pt layer. It is an important issue to properly separate the $V^{\text{FM}}_{\text{ANE-ARLE}}$ and $V^{\text{FM-AFM}}_{\text{ISHE}}$ in metallic FM-AFM systems, but this is beyond the scope of the present paper.

Examining the thermal loop of the YIG/Cu(3 nm)/Co-Pt(5 nm)/Ir-Mn(8 nm) sample shown in Fig. 4(a), one notes that the V_{ISHE} reaches 0.77 μV, about twice of the value for the pseudo-SV with the same Cu and Co-Pt thicknesses. The Co-Pt spin-diffusion length is about 2.1 nm obtained from the pseudo-SV samples. One can estimate that about 10% spin current from the YIG can pass though the 5-nm Co-Pt layer into the Ir-Mn layer. With $\theta_{\text{SH(Ir-Mn)}} \approx 0.8\theta_{\text{SH(Pt)}}$ [37] and $\theta_{\text{SH(Co-Pt)}} \approx 0.2\theta_{\text{SH}(Pt)}$, $\lambda_{\text{SD(Ir-Mn)}} \approx 0.7$ nm [36] and $\lambda_{\text{SD(Co-Pt)}} \approx 2.1$ nm, and $\rho_{\text{(Ir-Mn)}} \approx 5\rho_{\text{(Co-Pt)}}$, we obtain $V^{\text{YIG/Ir-Mn}}_{\text{ISHE}} \approx 0.5\ \text{V}^{\text{YIG/Co-Pt}}_{\text{ISHE}}$ for the 5-nm Co-Pt SV sample by using Eq. (4). The much smaller ISHE voltage in the Ir-Mn layer generated from the YIG spin current definitely does not account for the observed large enhancement in V_{ISHE}. We emphasize that the spin current flowing in the Co-Pt layer for both the pseudo-SV and exchange-bias SV samples includes the spin current coming from the YIG and produced by the Co-Pt itself as well as the reflected counterpart, if any. In the pseudo-SV structure, the total spin current vanishes at the Co-Pt surface [42,43], which can be taken as the result of the spin-current reflection at the surface. The reflected spin current diffuses backwards and partially cancels the forward spin current coming from the YIG if the Co-Pt thickness is comparable to its spin-diffusion length. In contrast, since the AFM Ir-Mn has a large spin Hall angle with very short spin-diffusion length [36,37], the Ir-Mn layer in the SV structure can absorb most spin current coming from the YIG and the Co-Pt with negligible spin-current reflection. It is this spin-sinking effect that leads to the great enhancement of the ISHE voltage in the 5-nm Co-Pt SV sample. As for the YIG/Cu(3 nm)/Co-Pt(10 nm)/Ir-Mn(8 nm) sample shown in Fig. 4(b), the V_{ISHE} is directly determined to be about 0.30 μV, still

slightly larger than the corresponding value (0.28 μV) for the pseudo-SV of YIG/Cu(3 nm)/Co-Pt(10 nm). The YIG spin current is mostly consumed within the 10-nm Co-Pt layer with less than 1% reaching the Ir-Mn layer. Undoubtedly, the $V_{\mathrm{ISHE}}^{\mathrm{YIG/Ir\text{-}Mn}}$ is negligible in this relatively thick Co-Pt sample. However, the forward spin current produced by the Co-Pt can be taken as a constant. The elimination of the reflection of the spin current purely produced by the Co-Pt is still effective to gain a relatively larger V_{ISHE} after overcoming the voltage reduction caused by the Ir-Mn shunting. We stress that for conventional YIG/heavy NM heterostructures, a spin-sinking layer addition [44] should take effect in a much-shortened thickness range (with respect to the spin-diffusion length) because the NM itself does not generate spin current under the thermal gradient. Considering the pinning effect, the metallic FM-AFM bilayer structure is an efficient spin-current detector, superior to single metallic FM layers.

From Figs. 4(a) and 4(b), one can also obtain $V_{\mathrm{ANE\text{-}like}} \approx 1.59$ and 2.04 μV for the 5- and 10-nm SV sample, respectively. However, the $V_{\mathrm{ANE\text{-}like}}$ is 1.06 μV obtained in GGG/Cu(3 nm)/Co-Pt(5 nm)/Ir-Mn(8 nm), and 1.68 μV in GGG/Cu(3 nm)/Co-Pt(10 nm)/Ir-Mn(8 nm), and both values are slightly smaller than those determined from the corresponding SV samples. The spin accumulation in Cu and Co-Pt layers induced by YIG [42,43] probably enhances the $V_{\mathrm{ANE}}^{\mathrm{Co\text{-}Pt}}$ and, thus, the $V_{\mathrm{ANE\text{-}like}}$ value. Parenthetically, the ANE-like subloop of the YIG/Cu(3 nm)/Co-Pt(5 nm)/Ir-Mn(8 nm) sample in Fig. 4(a) is slightly slanted together with a smaller exchange-bias field of $H_{\mathrm{ex}} = -128$ Oe in comparison with the square ANE-like loop of the GGG/Cu(3 nm)/Co-Pt(5 nm)/Ir-Mn(8 nm) sample with $H_{\mathrm{ex}} = -175$ Oe in Fig. 4(c). This difference should be attributed mainly to the interlayer coupling as we mention earlier. For the thicker Co-Pt samples, the effect of interlayer coupling becomes less significant, as illustrated in Figs. 4(b) and 4(d).

In principle, the exchange-biased SV heterostructure should be applicable to any thin soft magnetic film of Fe, Ni, Co, CoFe, NiFe, or (Co,Fe)B, etc. Therefore, the ISHE of the soft Co film is finally examined through the SV heterostructure. Figure 5(a) shows the field dependence of thermal voltage (V_{th}) for the YIG/Cu(3.5 nm)/Co(5 nm)/Ir-Mn(8 nm) sample. The SV-like thermal voltage loop is evident with separated ISHE and ANE-like signals. It rather resembles the result of YIG/Cu(3.5 nm)/Co-Pt(5 nm)/Ir-Mn(8 nm) displayed in Fig. 5(b), except that the Co SV sample exhibits a much smaller coercivity for the ANE-like subloops. The Co SV sample presents $V_{\mathrm{ISHE}} = 0.25$ μV and $V_{\mathrm{ANE\text{-}like}} = 0.33$ μV, whereas the corresponding Co-Pt sample gives $V_{\mathrm{ISHE}} = 0.84$ μV and $V_{\mathrm{ANE\text{-}like}} = 1.04$ μV. Assuming a similar spin-diffusion length for Co and Co-Pt and, thus, a similar $V_{\mathrm{ISHE}}^{\mathrm{YIG/Ir\text{-}Mn}}$ for the Co and Co-Pt SV samples, we estimate $V_{\mathrm{ISHE(Co)}}^{p} \approx 0.22$ μV, $V_{\mathrm{ISHE(Co\text{-}Pt)}}^{p} \approx 0.83$ μV, $\rho_{\mathrm{(Co)}} \approx 17.4$ $\mu\Omega$ cm, and

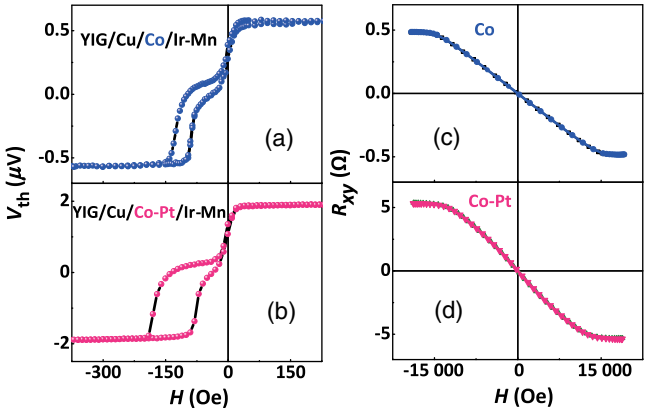

FIG. 5. Field dependence of thermal voltage V_{th} for (a) YIG/Cu(3.5 nm)/Co(5 nm)/Ir-Mn(8 nm) and (b) YIG/Cu (3.5 nm)/Co-Pt(5 nm)/Ir-Mn(8 nm). Anomalous Hall loops for (c) 5-nm Co film and (d) 5-nm Co-Pt film.

$\rho_{\mathrm{(Co\text{-}Pt)}} \approx 53.1$ $\mu\Omega$ cm. Using Eq. (4), we obtain $\theta_{\mathrm{SH(Co\text{-}Pt)}} \approx 1.1\theta_{\mathrm{SH(Co)}}$. As expected, the spin Hall angle of Co is enhanced when it is alloyed with Pt. Since the ISHE in FM metals is taken as the inverse effect of the AHE [45], the AHE of Co and Co-Pt films is further compared. Figures 5(c) and 5(d) depict the AHE loops of 5-nm Co and 5-nm Co-Pt films, respectively. Note that the AHE resistance of the Co-Pt film is about 10 times larger than that of the Co film. With the resistivity $\rho_{\mathrm{(Co\text{-}Pt)}} \approx 3.1$ $\rho_{\mathrm{(Co)}}$, we obtain the anomalous Hall angle relation of $\theta_{\mathrm{AH(Co\text{-}Pt)}} \approx 3.3\theta_{\mathrm{AH(Co)}}$. Apparently, the anomalous Hall angle of Co is also enhanced but by a larger factor. Our results imply that FM metals alloyed with a heavy element like Pt are beneficial to the ISHE and the AHE. The discrepancy between θ_{SH} and θ_{AH} may partly ascribe to the over-simplified assumptions in the θ_{SH} calculation. It is worth further exploring the quantitative relationship between ISHE and AHE in FM metals, but this is beyond the scope of the present paper.

IV. CONCLUSION

In summary, we investigate the ISHE of FM metals through the pseudo- and exchange-biased SVs based on YIG heterostructures with the longitudinal SSE configuration. The thin Co-Pt films exhibit quite large ISHE signals isolated from the ANE-ARLE signals in the heterostructures. The AFM Ir-Mn can not only magnetically pin the metallic FM layer but also lead to large enhanced ISHE signals due to the reduced spin-current reflection at the metallic FM surface because of the AFM spin sinking. We also find large enhancement of the ISHE and the AHE in Co films through alloying with Pt with large spin-orbit interaction. Our results suggest that the exchange-bias structure can be an effective approach to detect spin current, which provides insights into engineering sophisticated hybrid heterostructures for the generation,

manipulation, and detection of pure spin current for potential applications.

ACKNOWLEDGMENTS

This work is supported by National Key Research and Development Program of China under Grant No. 2016YFA0300804, the National Basic Research Program of China under Grant No. 2015CB921403, and the National Natural Science Foundation of China under Grants No. 51371191 and No. 51431009.

[1] S. O. Valenzuela and M. Tinkham, Direct electronic measurement of the spin Hall effect, Nature (London) **442**, 176 (2006).
[2] N. Okamoto, H. Kurebayashi, T. Trypiniotis, I. Farrer, D. A. Ritchie, E. Saitoh, J. Sinova, J. Mašek, T. Jungwirth, and C. H. W. Barnes, Electric control of the spin Hall effect by intervalley transitions, Nat. Mater. **13**, 932 (2014).
[3] K. Roy, Ultra-low-energy computing paradigm using giant spin Hall devices, J. Phys. D **47**, 422001 (2014).
[4] Y. Tserkovnyak and A. Brataas, Enhanced Gilbert Damping in Thin Ferromagnetic Films, Phys. Rev. Lett. **88**, 117601 (2002).
[5] B. Heinrich, C. Burrowes, E. Montoya, B. Kardasz, E. Girt, Y.-Y. Song, Y. Sun, and M. Wu, Spin Pumping at the Magnetic Insulator (YIG)/Normal Metal (Au) Interfaces, Phys. Rev. Lett. **107**, 066604 (2011).
[6] A. Azevedo, O. Alves Santos, G. A. Fonseca Guerra, R. O. Cunha, R. Rodríguez-Suárez, and S. M. Rezende, Competing spin pumping effects in magnetic hybrid structures, Appl. Phys. Lett. **104**, 052402 (2014).
[7] G. E. W. Bauer, E. Saitoh, and B. J. van Wees, Spin caloritronic, Nat. Mater. **11**, 391 (2012).
[8] K. Uchida, S. Takahashi, K. Harii, J. Ieda, W. Koshibae, K. Ando, S. Maekawa, and E. Saitoh, Observation of the spin Seebeck effect, Nature (London) **455**, 778 (2008).
[9] K. Uchida, J. Xiao, H. Adachi, J. Ohe, S. Takahashi, J. Ieda, T. Ota, Y. Kajiwara, H. Umezawa, H. Kawai, G. E. W. Bauer, S. Maekawa, and E. Saitoh, Spin Seebeck insulator, Nat. Mater. **9**, 894 (2010).
[10] C. M. Jaworski, J. Yang, S. Mack, D. D. Awschalom, J. P. Heremans, and R. C. Myers, Observation of the spin-Seebeck effect in a ferromagnetic semiconductor, Nat. Mater. **9**, 898 (2010).
[11] S. Y. Huang, W. G. Wang, S. F. Lee, J. Kwo, and C. L. Chien, Intrinsic Spin-Dependent Thermal Transport, Phys. Rev. Lett. **107**, 216604 (2011).
[12] A. D. Avery, M. R. Pufall, and B. L. Zink, Observation of the Planar Nernst Effect in Permalloy and Nickel Thin Films with In-Plane Thermal Gradients, Phys. Rev. Lett. **109**, 196602 (2012).
[13] D. Meier, D. Reinhardt, M. Schmid, C. H. Back, J.-M. Schmalhorst, T. Kuschel, and G. Reiss, Influence of heat flow directions on Nernst effects in Py/Pt bilayers, Phys. Rev. B **88**, 184425 (2013).
[14] M. Schmid, S. Srichandan, D. Meier, T. Kuschel, J.-M. Schmalhorst, M. Vogel, G. Reiss, C. Strunk, and C. H. Back, Transverse Spin Seebeck Effect versus Anomalous and Planar Nernst Effects in Permalloy Thin Films, Phys. Rev. Lett. **111**, 187201 (2013).
[15] J.-E. Wegrowe, D. Lacour, and H.-J. Drouin, Anisotropic magnetothermal transport, and spin Seebeck effect, Phys. Rev. B **89**, 094409 (2014).
[16] B. Madon, Do Ch. Pham, J.-E. Wegrowe, D. Lacour, M. Hehn, V. Polewczyk, A. Anane, and V. Cros, Anomalous and planar Righi-Leduc effects in $Ni_{80}Fe_{20}$ ferromagnets, Phys. Rev. B **94**, 144423 (2016).
[17] S. Y. Huang, X. Fan, D. Qu, Y. P. Chen, W. G. Wang, J. Wu, T. Y. Chen, J. Q. Xiao, and C. L. Chien, Transport Magnetic Proximity Effects in Platinum, Phys. Rev. Lett. **109**, 107204 (2012).
[18] Y. M. Lu, Y. Choi, C. M. Ortega, X. M. Cheng, J. W. Cai, S. Y. Huang, L. Sun, and C. L. Chien, Pt Magnetic Polarization on $Y_3Fe_5O_{12}$ and Magnetotransport Characteristics, Phys. Rev. Lett. **110**, 147207 (2013).
[19] T. Kikkawa, K. Uchida, Y. Shiomi, Z. Qiu, D. Hou, D. Tian, H. Nakayama, X. F. Jin, and E. Saitoh, Longitudinal Spin Seebeck Effect Free from the Proximity Nernst Effect, Phys. Rev. Lett. **110**, 067207 (2013).
[20] D. Qu, S. Y. Huang, J. Hu, R. Wu, and C. L. Chien, Intrinsic Spin Seebeck Effect in Au/YIG, Phys. Rev. Lett. **110**, 067206 (2013).
[21] L. K. Zou, S. H. Wang, Y. Zhang, J. R. Sun, J. W. Cai, and S. S. Kang, Large extrinsic spin Hall effect in Au-Cu alloys by extensive atomic disorder scattering, Phys. Rev. B **93**, 014422 (2016).
[22] K. Uchida, M. Ishida, T. Kikkawa, A. Kirihara, T. Murakami, and E. Saitoh, Longitudinal spin Seebeck effect: From fundamentals to applications, J. Phys. Condens. Matter **26**, 343202 (2014).
[23] B. F. Miao, S. Y. Huang, D. Qu, and C. L. Chien, Inverse Spin Hall Effect in a Ferromagnetic Metal, Phys. Rev. Lett. **111**, 066602 (2013).
[24] S. M. Wu, J. Hoffman, J. E. Pearson, and A. Bhattacharya, Unambiguous separation of the inverse spin Hall and anomalous Nernst effects within a ferromagnetic metal using the spin Seebeck effect, Appl. Phys. Lett. **105**, 092409 (2014).
[25] V. Cherepanov, I. Kolokolov, and V. L'vov, The saga of YIG: Spectra, thermodynamics, interaction and relaxation of magnons in a complex magnet, Phys. Rep. **229**, 81 (1993).
[26] A. V. Chumak, V. I. Vasyuchka, A. A. Serga, and B. Hillebrands, Magnon spintronics, Nat. Phys. **11**, 453 (2015).
[27] D. Tian, Y. Li, D. Qu, X. Jin, and C. L. Chien, Separation of spin Seebeck effect and anomalous Nernst effect in Co/Cu/YIG, Appl. Phys. Lett. **106**, 212407 (2015).
[28] M. Kitada and N. Shimizu, Magnetic properties of sputtered Co-Pt thin films, J. Appl. Phys. **54**, 7089 (1983).
[29] F. Bolzoni, F. Leccabue, R. Panizzieri, and L. Pareti, Magnetocrystalline anisotropy and phase transformation in Co-Pt alloy, IEEE Trans. Magn. **20**, 1625 (1984).
[30] W. H. Meiklejohn and C. P. Bean, New magnetic anisotropy, Phys. Rev. **102**, 1413 (1956).
[31] J. Nogués and I. K. Schuller, Exchange bias, J. Magn. Magn. Mater. **192**, 203 (1999).

[32] R. Coehoorn, in *Handbook of Magnetic Materials*, edited by K. H. J. Buschow (North-Holland, Amsterdam, 2003), Vol. 15, pp. 1–197.

[33] S. Parkin, X. Jiang, C. Kaiser, A. Panchula, K. Roche, and M. Samant, Magnetically engineered spintronic sensors and memory, Proc. IEEE **91**, 661 (2003).

[34] L. Frangou, S. Oyarzun, S. Auffret, L. Vila, S. Gambarelli, and V. Baltz, Enhanced Spin Pumping Efficiency in Antiferromagnetic Ir-Mn Thin Films around the Magnetic Phase Transition, Phys. Rev. Lett. **116**, 077203 (2016).

[35] W. Zhang, M. B. Jungfleisch, F. Freimuth, W. J. Jiang, J. Sklenar, J. E. Pearson, J. B. Ketterson, Y. Mokrousov, and A. Hoffmann, All-electrical manipulation of magnetization dynamics in a ferromagnet by antiferromagnets with anisotropic spin Hall effects, Phys. Rev. B **92**, 144405 (2015).

[36] W. Zhang, M. B. Jungfleisch, W. J. Jiang, J. E. Pearson, A. Hoffmann, F. Freimuth, and Y. Mokrousov, Spin Hall Effects in Metallic Antiferromagnets, Phys. Rev. Lett. **113**, 196602 (2014).

[37] J. B. S. Mendes, R. O. Cunha, O. Alves Santos, P. R. T. Ribeiro, F. L. A. Machado, R. L. Rodríguez-Suárez, A. Azevedo, and S. M. Rezende, Large inverse spin Hall effect in the antiferromagnetic metal $Ir_{20}Mn_{80}$, Phys. Rev. B **89**, 140406(R) (2014).

[38] D. E. Bürgler, P. Grünberg, S. O. Demokritov, and M. T. Johnson, in *Handbook of Magnetic Materials*, edited by K. H. J. Buschow (North-Holland, Amsterdam, 2003), Vol. 13, pp. 13–29.

[39] D. Qu, S. Y. Huang, B. F. Miao, S. X. Huang, and C. L. Chien, Self-consistent determination of spin Hall angles in selected 5*d* metals by thermal spin injection, Phys. Rev. B **89**, 140407(R) (2014).

[40] H. L. Wang, C. H. Du, Y. Pu, R. Adur, P. C. Hammel, and F. Y. Yang, Scaling of Spin Hall Angle in 3*d*, 4*d*, and 5*d* Metals from $Y_3Fe_5O_{12}$/Metal Spin Pumping, Phys. Rev. Lett. **112**, 197201 (2014).

[41] A. Scholl, M. Liberati, E. Arenholz, H. Ohldag, and J. Stöhr, Creation of an Antiferromagnetic Exchange Spring, Phys. Rev. Lett. **92**, 247201 (2004).

[42] M. Schreier, A. Kamra, M. Weiler, J. Xiao, G. E. W. Bauer, R. Gross, and S. T. B. Goennenwein, Magnon, phonon, and electron temperature profiles and the spin Seebeck effect in magnetic insulator/normal metal hybrid structures, Phys. Rev. B **88**, 094410 (2013).

[43] H. J. Jiao and G. E. W. Bauer, Spin Backflow and ac Voltage Generation by Spin Pumping and the Inverse Spin Hall Effect, Phys. Rev. Lett. **110**, 217602 (2013).

[44] H. Ulrichs, V. E. Demidov, S. O. Demokritov, W. L. Lim, J. Melander, N. Ebrahim-Zadeh, and S. Urazhdin, Optimization of Pt-based spin-Hall-effect spintronic devices, Appl. Phys. Lett. **102**, 132402 (2013).

[45] N. Nagaosa, J. Sinova, S. Onoda, A. H. MacDonald, and N. P. Ong, Anomalous Hall effect, Rev. Mod. Phys. **82**, 1539 (2010).